AGU PUBLICATIONS

JGR

Journal of Geophysical Research: Oceans

RESEARCH ARTICLE

10.1002/2014JC010218

Special Section:
Pacific-Asian Marginal Seas

Winter bloom and associated upwelling northwest of the Luzon Island: A coupled physical-biological modeling approach

Wenfang Lu[1,2], Xiao-Hai Yan[1,2], and Yuwu Jiang[1]

[1]State Key Laboratory of Marine Environmental Science, Xiamen University, Xiamen, China, [2]College of Earth, Ocean, and Environment, University of Delaware, Newark, Delaware, USA

Key Points:
- Winter bloom in Luzon Strait is studied with physical-biological model
- Wind-induced mixing and upwelling jointly responsible for nutrient supply
- The mechanism of subsurface upwelling is mainly vorticity advection

Correspondence to:
Y. Jiang,
ywjiang@xmu.edu.cn

Citation:
Lu, W., X.-H. Yan, and Y. Jiang (2015), Winter bloom and associated upwelling northwest of the Luzon Island: A coupled physical-biological modeling approach, *J. Geophys. Res. Oceans*, *120*, 533–546, doi:10.1002/2014JC010218.

Received 16 JUN 2014
Accepted 24 DEC 2014
Accepted article online 30 DEC 2014
Published online 29 JAN 2015

Abstract For this paper, a coupled physical-biological model was developed in order to study the mechanisms of the winter bloom in the Luzon Strait (referred as LZB). Based on a simulation for January 2010, the results showed that the model was capable of reproducing the key features of the LZB, such as the location, inverted-V shape, twin-core structure and bloom intensity. The simulation showed that the LZB occurred during the relaxation period of intensified northeasterly winds, when the deepened mixed layer started to shoal. Nutrient diagnostics showed that vertical mixing was responsible for the nutrient supply to the upper ~40 m layer, while subsurface upwelling supplied nutrients to the region below the mixed layer. Hydrodynamic diagnostics showed that the advection of relative vorticity (RV) primarily contributed to the subsurface upwelling. The RV advection was resulted from an offshore jet, which was associated with a northeasterly wind, flowed across the ambient RV field.

1. Introduction

The South China Sea (SCS) is the largest marginal sea in the western Pacific Ocean. The Luzon Strait (LS), located in the SCS, is a major channel that allows significant water mass exchange with the open ocean. The surface circulation in the SCS is predominantly controlled by the East Asian Monsoon, which has southwesterly winds in the summer, from June to September, and strong northeasterly winds from November to March [*Liu et al*., 2002]. Because basin-scale gyres in the surface circulation isolate the interior water of the SCS, this area is characterized by oligotrophic properties, despite terrestrial inputs from several rivers [*Wong et al*., 2007].

The LS is located between Taiwan Island and Luzon Island (LI) and has a sill depth of ~1900 m [*Liu et al*., 2002]. The Manila Trench is located west of the LS. The Kuroshio flows northward but frequently penetrates into the SCS in the middle of the LS [*Wang et al*., 2012]. The Kuroshio loop current (marked K in Figure 1b) drives both cyclonic and anticyclonic mesoscale eddies in the vicinity of the LS through eddy shedding [*Wu and Chiang*, 2007; *Metzger and Hurlburt*, 2001; *Wang et al*., 2003]. The riverine influences from the Cagayan River (CR in Figure 1b) and the Gaoping River (GR in Figure 1b) are localized relative to the Kuroshio influence.

Winter Luzon Blooms (LZB, approximately located in the red circle of Figure 1b), which have been confirmed by many observational and remote sensing studies, occasionally appear northwest of LI. In contrast with common spring phytoplankton blooms over the continental shelf [e.g., *Sverdrup*, 1953; *Townsend et al*., 1992], the LZB usually flourishes in winter over water depths greater than 2500 m [*Tang et al*., 1999]. In the oligotrophic SCS, blooms impact the productivity of the local marine ecosystem, and hence on ocean carbon flux [*Townsend et al*., 1992]. Moreover, studying the dynamics of the LZB will improve understanding of the complex biogeochemical processes near the LS. The remarkable spatial and temporal specificities and significances of the LZB prompted the oceanography community to investigate this phenomenon.

Shaw et al. [1996] discovered the subsurface upwelling off the northeastern coast of LI from hydrologic data taken in December 1990. From the pigment concentration results of historical Coastal Zone Color Scanner (CZCS) data from 1979 to 1986, *Tang et al*. [1999] found that the LZB occurred in December 1979, February 1983, February 1985, and January 1986, demonstrating that this phenomenon is not an infrequent occurrence in the LS in winter. *Shang et al*. [2012] proposed that the bloom generally persists from November to February, and peaks in December. *Peñaflor et al*. [2007] showed that the LZB reached its maximum intensity

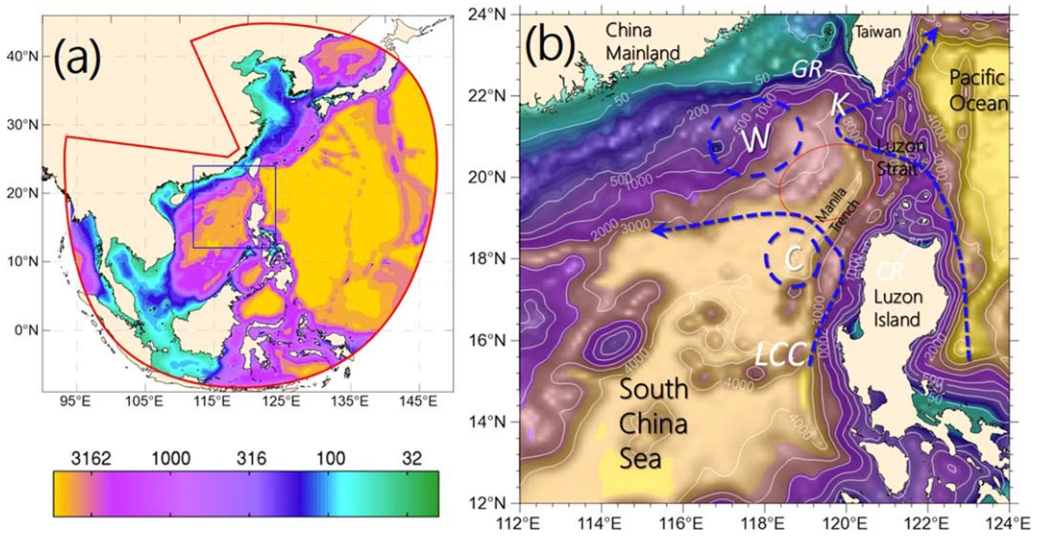

Figure 1. (a) Model domain within bold red lines. Blue box is the region of Figure 1b. (b) The model bathymetry (shading map, unit: meter) of Northern South China Sea in the vicinity of Luzon Strait. White contours indicate the isobaths of 50, 200, 500, 1000, 2000, 3000, and 4000 m. Blue bold-dashed lines show the major dynamic processes near Luzon Strait in January 2010, while white italic abbreviations mean: W: warm-core eddy; K: Kuroshio; CR: Mouth of Cagayan River; GR: Mouth of Gaoping River; LCC: Luzon Coastal Current; C: Cold-core eddy. Red circle denotes the approximate extent of the Luzon Bloom found in previous studies.

in early spring with approximate chlorophyll concentrations of 2.0 mg m^{-3}. Using an analytically derived phytoplankton absorption coefficient (Aph), *Shang et al.* [2012] revealed the explicit inverted-V and two-wing (nearshore and offshore) structure of the LZB from MODIS satellite images. The nearshore wing of the LZB was investigated for the first time by *Peñaflor et al.* [2007] and they attributed its structure to lee effects from the Kuroshio flowing past Luzon Island. For the offshore bloom patch, possible nutrient sources proposed by *Tang et al.* [1999] were (1) remote advection from the nearshore, (2) local upwelling by fronts or eddy processes or (3) enhanced vertical mixing; among these the contribution from local upwelling was highlighted.

Many different mechanisms for the offshore bloom have been proposed and discussed. *Chen et al.* [2006] inferred from in situ data that a shallower MLD in winter was associated with upwelling caused by Ekman pumping. *Wang et al.* [2010] found that the MLD, which was derived from NASA's Ocean Biogeochemical Model (NOBM), became deeper in winter, and classical Ekman pumping theory was highlighted to be responsible for the LZB in collaboration with wind-induced mixing. In addition to the wind-induced upwelling mechanism, Kuroshio loops across the middle of the LS could also be responsible for the LZB [*Peñaflor et al.*, 2007; *Shang et al.*, 2012]. Local upwelling related to Kuroshio-eddy interaction or Kuroshio-topography effects can be deduced from remote sensing evidence [*Shang et al.*, 2012]. *Peñaflor et al.* [2007] proposed that the LZB was associated with the interaction between Kuroshio and the basin circulation; however, the underlying mechanism was not yet clear. *Shaw et al.* [1996] noted that the driving force for the upwelling was associated with the subbasin-scale deep circulation, namely the Luzon Coastal Current (LCC) reported by *Fang et al.* [1998] and *Hu et al.* [2000]. This genesis mechanism was also invoked by *Liu et al.* [2002]. Beyond the above effects, eddy pumping effects on the LZB was also highlighted by *Chen et al.* [2007]. The dynamics of SCS was characterized by vigorous eddy activity with eddy-generated vertical exchanges playing an essential role in the upper ocean ecosystem [*Klein and Lapeyre*, 2009]. Eddy activity in this area may dramatically modify the vertical distribution and horizontal pattern of nutrients, thereby affecting productivity.

Based on previous literature, the mechanisms of the LZB and its relation with upwelling are still under debate, which motivated us to investigate and discuss this phenomenon. Because time and space limitations exist (e.g., cloud contamination or weather constraints), neither episodic remote sensing images nor relatively static in situ observations will allow us to fully understand the mechanisms of the LZB. In order to analyze and reveal the complex physical mechanisms from a hydrodynamic viewpoint, and to further understand the biogeochemical processes, we employed a three-dimensional physical-biological coupled

model in this study. The objectives of this study were (1) to examine the role of various physical processes (e.g., northeasterly monsoon, coastal current, Kuroshio loop current and eddy activities) on the LZB in a realistic ocean scenario; (2) to provide dynamic interpretation for the conceptual mechanism models in previous studies [*Peñaflor et al*., 2007; *Wang et al*., 2010] and (3) to gain insights into the triggering and sustaining factors of the LZB, as well as into the biogeochemical system in the vicinity of the LS. We chose to study the bloom in January 2010 and, in particular, to focus on the mesoscale processes on the week to month time scales. The January 2010 bloom was a typical scenario when compared with those instances from *Wang et al*. [2010] and *Tang et al*. [1999].

This paper is organized as follows: In section 2, the model configuration and remote sensing data used in this study are described. In section 3, we present the model outputs and compare them with remote sensing data as validation. In addition, we show a series of model results, including horizontal distributions, vertical profiles, and wind-induced processes. In section 4, we use the nutrient diagnostics method to comprehensively analyze the mechanisms that are active in the LZB. To further discuss the mechanisms of subsurface upwelling, we employ the vorticity equation to diagnose hydrodynamics of the system. Finally, the conclusions and prospects are summarized in section 5.

2. Model and Methods

2.1. Model Configuration

The physical-biological coupled model employed in this study was based on the Regional Ocean Model System (ROMS). ROMS is a free-surface, hydrostatic ocean model solving the primitive equations on topography-following coordinates [*Shchepetkin and McWilliams*, 2005]. The physical model was from the operational Taiwan Strait Nowcast\Forecast system (TFOR), which provides multipurpose oceanic simulations [*Jiang et al*., 2011; *Liao et al*., 2013; *Wang et al*., 2013]. Although the orthogonal curvilinear grid of TFOR (Figure 1a) was centered in the Taiwan Strait, the spatial resolution in the vicinity of LS was finer than 10 km and was adequate for the scope of this study. The model bathymetry was a combination of the ETOPO2v2 data set and digitized depth data published by the China Maritime Safety Administration. A vertical topography-following S coordinate was adopted with 30 σ-layers. In the open boundary, the boundary conditions were derived from the *My Ocean Project* (http://www.myocean.eu/) data. The daily atmospheric forcing data (i.e., wind stress, net heat flux and fresh water flux) used in this study were from the Weather Research and Forecasting model (WRF) operated in the Fujian Marine Forecasting Institute (http://www.fjmf.gov.cn/NumPrediction/NumericalPrediction.aspx). The mixing parameterization scheme used was the Mellor-Yamada's level 2.5 turbulence closure model [*Mellor and Yamada*, 1982]. Our sensitivity tests suggested that tidal effects were not a significant contributor to the LZB, so we excluded tidal forcing from the model (not shown in figures). Monthly mean discharges from the major rivers were added to the domain as point sources of water and tracers, with the Cagayan River input specified by data from the SAGE River Discharge Database (http://www.sage.wisc.edu/riverdata/).

The biological model, on the other hand, was described in *Wang et al*. [2013], which was based on the nitrogen-based, nutrient-phytoplankton-zooplankton-detritus (NPZD) model by *Fennel et al*. [2006]. The model was composed of nitrate (NO_3), ammonium (NH_4), large detritus, small detritus, phytoplankton, zooplankton and chlorophyll. The initial fields and boundary conditions for the biological tracers were derived from the World Ocean Atlas 2005 (WOA2005) database (http://www.nodc.noaa.gov/OC5/WOA05/pr_woa05.html). The detailed configuration and parameter values as well as the validation and skill assessment were discussed in *Liao et al*. [2013] and *Wang et al*. [2013].

2.2. Remote Sensing Data

Daily Aqua MODIS level-3 chlorophyll (9 km resolution) and Terra MODIS level-3 SST (daytime, 4 km resolution) images for 28 January 2010 were obtained from the NASA Distributed Active Archive Center (DAAC, http://oceancolor.gsfc.nasa.gov/). Climatological January SST data (4 km resolution) were also obtained from the Aqua MODIS satellite level-3 products. The Mean Dynamic Topography (MDT_CNES-CLS09, v1.1 version) altimeter product from 1993 to 2010 was produced by the *CLS* Space Oceanography Division (http://www.aviso.oceanobs.com/), while the gridded Absolute Dynamic Topography (ADT, 1/3° resolution) was from the Jason-2 satellite, which was averaged weekly from 27 January to 2 February 2010, and the climatological Sea Level Anomaly (SLA, 1/4° resolution) was produced by Ssalto/*Duacs* (http://www.aviso.

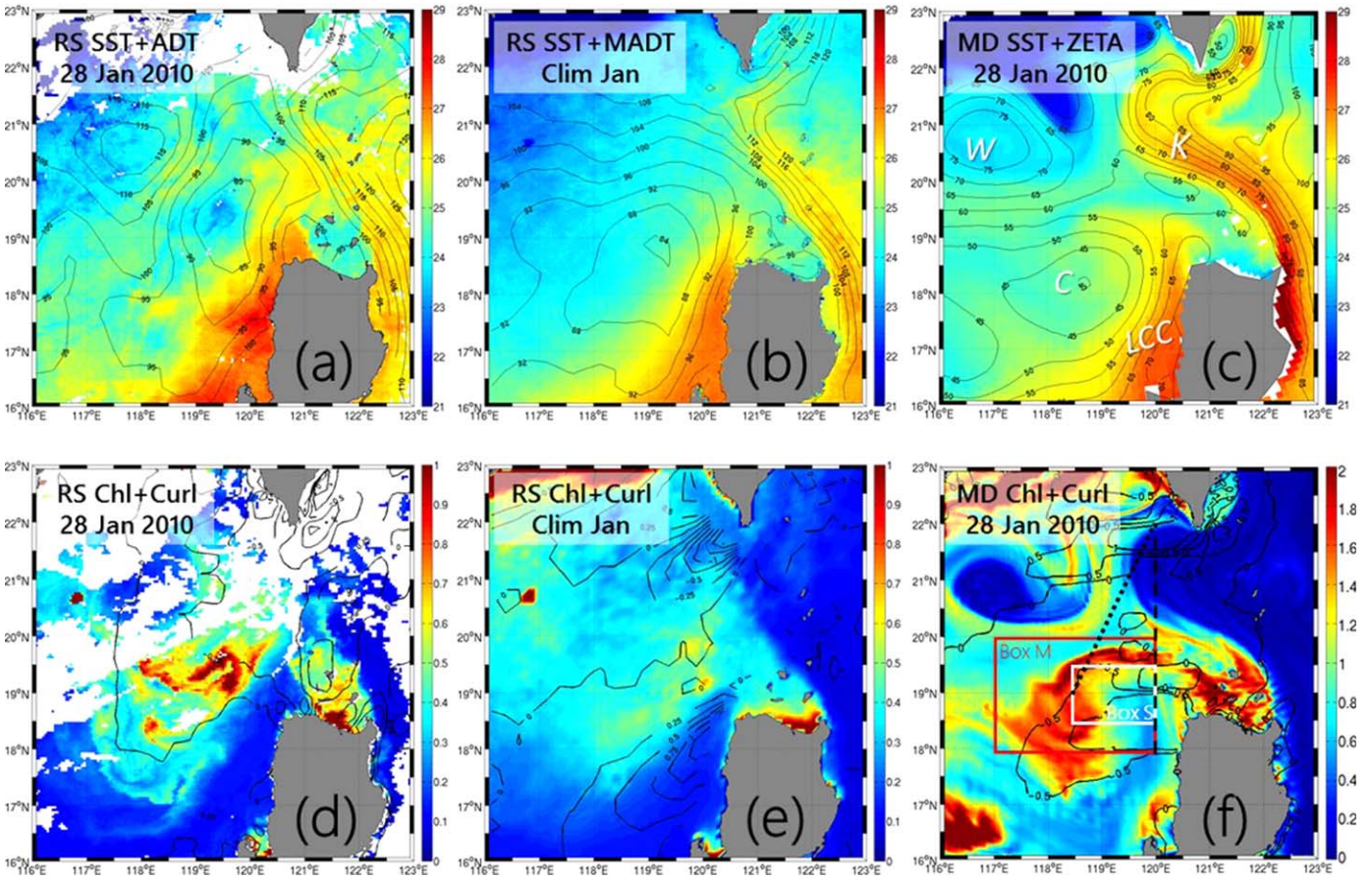

Figure 2. (top) (a–c) plane view of SST (color, unit: °C) with contours of the associated sea surface height (ADT from remote sensing data and surface elevation from the model). (bottom) (d–f) SSC concentration (color, unit: mg L^{-3}) with contours of the associated wind curl (unit: $\times 10^{-6}$ s^{-1}). (a) SST on 28 January with weekly mean ADT contours (unit: cm) from 27 January to 2 February 2010. (b) SST and mean ADT contours from climatological January. (c) Model SST with contours of SSH (unit: cm); (d) MODIS SSC concentration and contours of QuikSCAT wind curl on 28 January 2010. (e) Same as Figure 2d, but for climatological January. (f) Modeled SSC and contours of wind stress curl on 28 January. Box M (in red) and Box S (in white) are the areas over which spatial averaging is performed in the following figures, while the dashed line denotes the position of the section presented in Figure 3. Dotted line is the location of the section from *Chen et al.* [2006]. White italic abbreviations in Figure 2c have the same meaning with those in Figure 1b.

oceanobs.com/duacs/). Both categories of data were distributed by *Aviso* with support from the Centre National d'Etudes Spatiales *(Cnes)*. The climatological January mean ADT (MADT) was computed from MDT and the climatological January SLA was linearly interpolated to eliminate resolution differences. The Sea-Winds scatterometer on the Quick Scatterometer (QuikSCAT) which had climatological averaged wind data for 2000–2007 (ftp://ftp.remss.com/qscat/bmaps_v04/, 1/4° resolution), was used to derive the wind stress curl near the LS.

3. Results

3.1. Horizontal Distribution of Tracers

The modeled general circulation pattern for January 2010 near the LS is shown in Figure 1b. Modeled sea surface temperature (SST) and sea surface chlorophyll (SSC) on 28 January 2010, are presented in Figures 2c and 2f, respectively, along with the remote sensing data for January 2010 (Figures 2a and 2d) and in the climatological January (Figures 2b and 2e), for comparison. In all scenarios, the Kuroshio bordered the eastern LS, which was characterized by SST over 27°C and was sustained by a high sea surface height (SSH) gradient. Among the three types of Kuroshio intrusion into SCS [*Nan et al.*, 2011], this scenario was likely to be the looping path. The Kuroshio clearly veers into the SCS across the middle of the LS and exits the SCS at the northern side of the LS, forming an anticyclonic Kuroshio loop. In winter time, the Kuroshio occasionally intrudes into the SCS and forms such a looping structure [*Wu and Chiang*, 2007; *Caruso et al.*, 2006]. The

presence of a warm-core eddy (marked "*W*" in Figure 2c) located at ~117°E, 20.5°N in the model can be observed from the high SSH and low SSC. Another significant feature shown in Figures 2a and 2c was the low SSH, low SST, and high productivity region of western LI. *Shang et al*. [2012] identified this phenomenon as cold-core eddy activity. In our model, the center of this cold-core eddy appeared at 118.6°E, 18.2°N (Labeled "*C*" in Figure 2c), with a warmer SST center relative to the observations. To the west of LI, the LCC, with higher temperature waters that were tracked back to the interior of the SCS, flowed northward to ~20°N [*Shaw et al*., 1996]. Constrained by the cold eddy, the LCC flowed northward and encountered the Kuroshio loop current, where a thermal front was observed on both sides of warm LCC water (Figure 2a). The modeled LCC, however, turned westward and penetrated back into the SCS, although a discernible thermal front was still apparent (Figure 2c). Excluding the warm-core eddy, the modeled SSC, SST, and SSH patterns, especially the LCC and the cold-core eddy, matched the climatological scenario quite well (Figures 2b and 2e).

While the model does not completely resolve the precise location and intensity (e.g., modeled SSC values were much higher than the remote sensing values) of the LZB, the key features of the bloom patch were

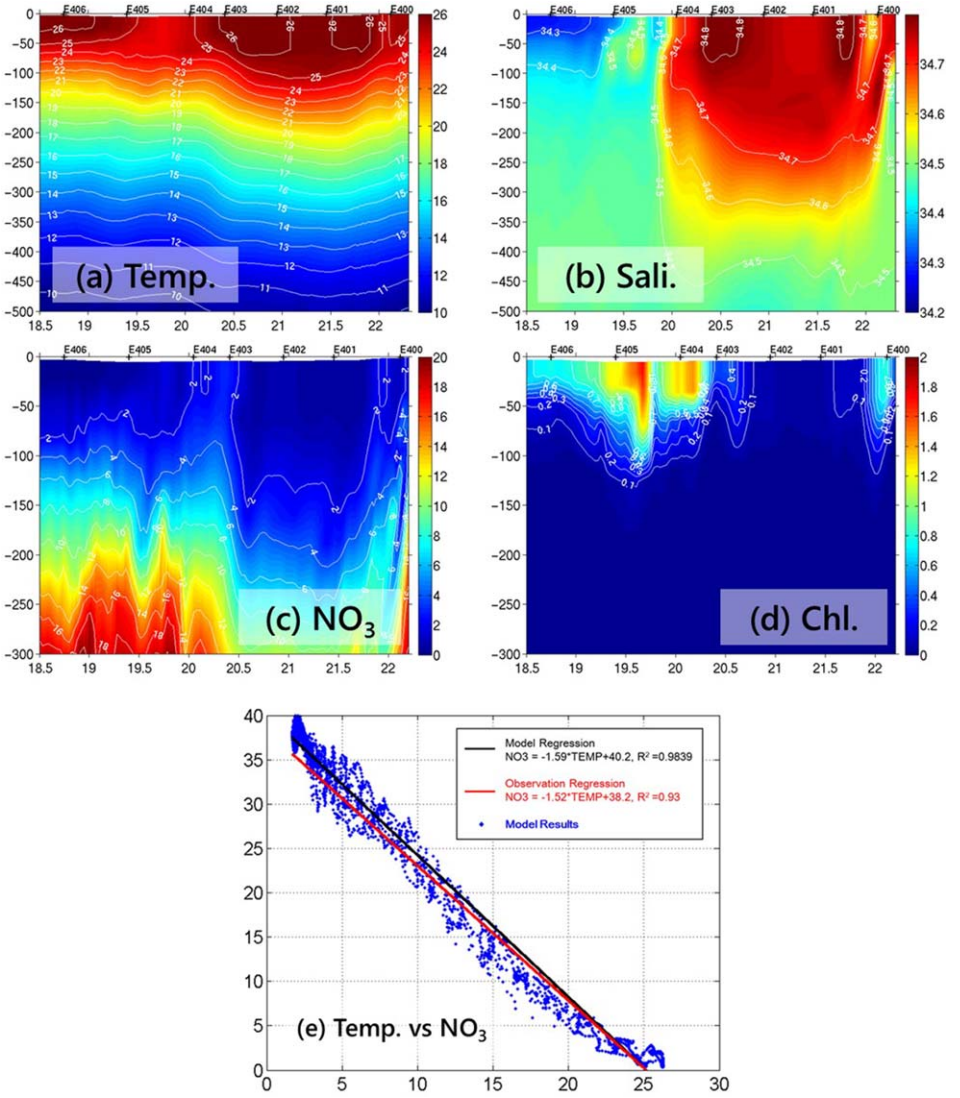

Figure 3. Model validation: (a) Modeled daily averaged temperature (unit: °C), (b) salinity, (c) nitrate concentration (unit: mmol m^{-3}) and (d) chlorophyll concentration (unit: mg m^{-3}) profiles for the along transect 120°E (refer to dash line in Figure 2f) on 28 January 2010. The cross marks above indicate the observation stations of *Shang et al*. [2012] (see their Figure 6c for observed profile plots). (e) Blue dots show modeled temperature versus NO_3 plot at section near LS (see dot line in Figure 2f) in January. Black line is the regression curve of modeled data, while red line shows the observed relation from *Chen et al*. [2006] (see their figure 7).

captured. For example, the area with high productivity formed an inverted-V shape, two-wing structure to the northwest of LI, which was consistent with the patterns found in other studies [*Peñaflor et al*., 2007; *Shang et al*., 2012]. The modeled intensity of the bloom was exaggerated, while the near-shore wing (to the north of LI) and the offshore wing (~200 km northwest of LI) were separately discernable. Moreover, the position of the bloom patch was located offshore to the north of the LCC. This feature implied that the LCC may have played a role in the LZB. The underlying implication of this will be discussed in the next section.

3.2. Vertical Distribution of Tracers

Figure 3 shows the vertical profiles of temperature, salinity, nitrate nutrient and chlorophyll on a section along 120°E (see Figure 2f for location) for validation. The cross marks above the profiles show approximate positions of corresponding stations from *Shang et al*. [2012]. The vertical temperature structures in observation and in the model were both well stratified, except within the surface mixing layer (~50 m deep). On the southern portion of the section, low salinity (fresher than 34.4) and high temperature (>25°C) water occurred from surface down to 50 m which originated from the interior of the SCS and was advected by the LCC. When comparing the northern and southern portions of the section, the isotherms in the south were uplifted ~50 m relative to the north. This pattern was inconsistent with the observations. In the salinity profile, high salinity water from the intrusive Kuroshio was as deep as 500 m. This signal was also clear in the observation, although the observational position was to the north of station E402. The small portion of high salinity water in the upper 100 m layer near 19.7°N was associated with an offshore jet. *Shang et al*. [2012] revealed two upward doming isotherms. In the model profiles, two domes were also discernable. One was located to the south of Kuroshio high salinity water, while the other was further south near station E405. The isotherms dome beneath the thermocline extended deeper than 500 m. In summary, our model was not completely resolve the vertical structure of temperature and salinity (e.g., the strong thermocline above 20°C isotherm), partially because of the limited vertical resolution; however, the model did capture the north-south contrast pattern in the LS and the two upward motions.

The vertical structure of NO_3 along the section (dot line in Figure 2f) near the LS was compared to that from *Chen et al*. [2006, Figure 7]. The regression curve of modeled temperature versus nitrate showed almost identical slopes and intercepts values (Figure 3e) with the observation. The modeled and observed high correlation coefficient (0.98 and 0.93) means that the variation of nitrate was highly related to that of temperature, therefore the physical modeling performance could almost decide the biological modeling nutrient estimation. At the two doming sites, the nitrate isolines showed significant uplift (Figure 3c). High productivity appeared on the north side of the jet at ~19.7° N (Figure 3d). The bloom patch was found at upper ~100 m layer and had a horizontal width of ~100 km. Generally, modeled nitrate, which is an essential biological parameter in nitrate-based system, agreed with the observations reported by *Chen et al*. [2006] reasonably.

3.3. Wind and Mixed Layer

Figures 4a and 4b are time series of spatially averaged wind stress. As seen from the expanded time series of wind stress magnitude, from the 14 to the 31 January, the wind strengthened and reached a peak value of approximately 0.37 Pa and persisted for more than half a month. Historical documents showed that the wind speed during the winter northeast monsoon in the SCS averaged approximately 9 m s^{-1} (~0.26 Pa) [*Wyrtki*, 1961]. The wind stress peaked on 17 January was approximately 1.4 times the mean value. Leading up to the 17 January peak, the local winds shifted to a primarily northerly direction as it strengthened (see Figure 4c). From 31 January onward, the wind weakened and switched to an easterly wind (Figure 4d). Northerly winds were upwelling-favorable to the west of LI. The multiple cores of wind curl (e.g., the two positive centers near the south cape of Taiwan and west of LI, Figure 2e), were caused by the orographic blocking effect of the mountains [*Wang et al*., 2008]. Such oscillations of the local wind will inevitably drive short temporal scale processes, e.g., intensification of wind-induced mixing or wind-induced upwelling, especially within a Rossby radius of deformation of LI and the Taiwan coast, which was approximately 50 km in the first baroclinic mode [*Chelton et al*., 1998].

In order to analyze the time variations of wind-induced processes, a 5 day moving average of the wind stress (Pa), mixed layer depth (MLD, unit: m), surface NO_3 (mmol m^{-3}) and SSC concentration (mg m^{-3}) were spatially averaged within Box M (see Figure 2f). Box M was deliberately selected to cover the dynamic core of the bloom patch, especially during its rapid growth. The time series are presented in Figure 5.

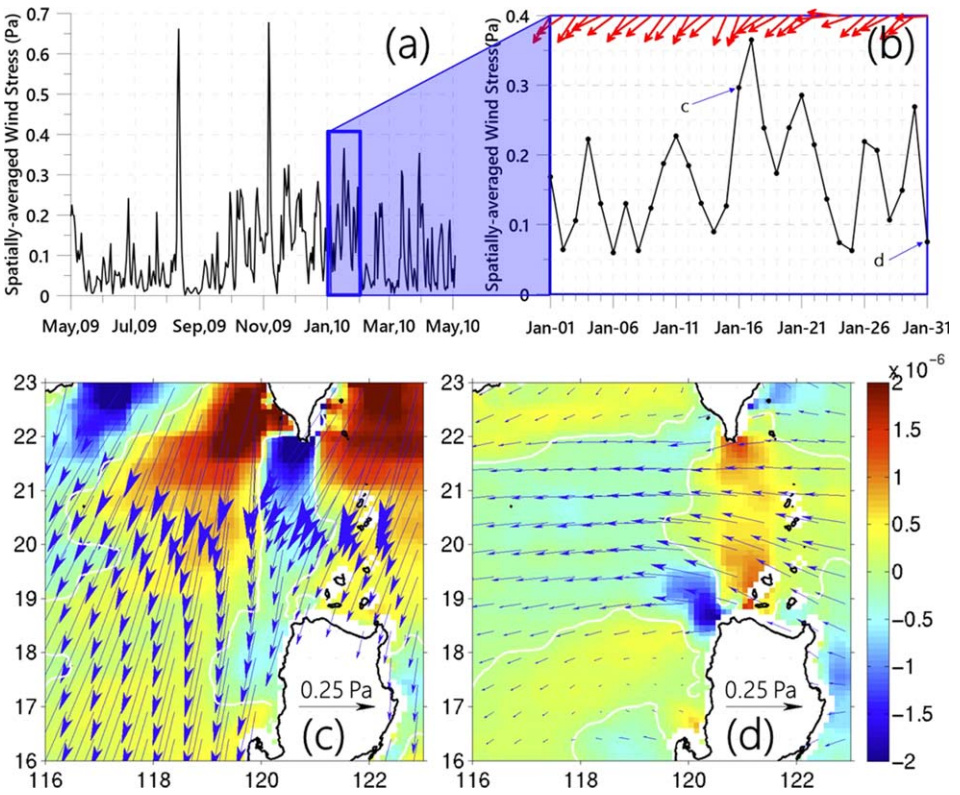

Figure 4. Winds near the LS. (a) Wind stress spatially averaged within the region in Figures 4c and 4d. (b) Expanded time series of wind stress for January 2010. Red vectors above are corresponding unit vectors of wind stress showing wind direction. Two distinctive wind patterns near the LS for (c) 16 January and (d) 31 January, respectively. Color shading in these maps is the wind stress curl (Pa m^{-1}) with the white contours showing the zero values.

Meanwhile, Figure 6 shows the time-depth maps of temperature, salinity, vertical velocity, NO_3 and phytoplankton, also averaged within Box M, as well as the time series of spatially averaged wind stress, vectors and surface phytoplankton concentration. In this section, we focused on the variability from January to mid-February.

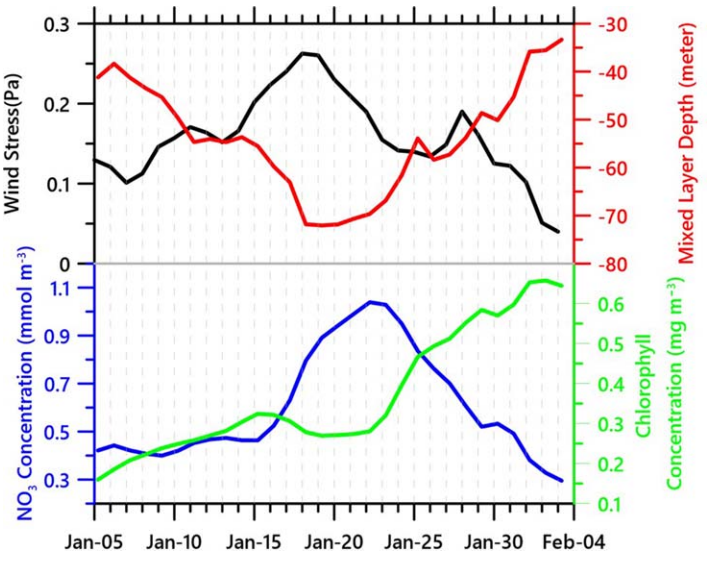

Figure 5. Time series, which are spatial averaged over Box M (shown in Figure 2f) in 2010, of: Black: 5 day moving averaged wind stress (Pa); Red: Mixed Layer Depth (meter); Blue: Surface NO_3 concentration (mmol m^{-3}); Green: SSC concentration (mg m^{-3}).

Following the wind intensification, MLD deepened from 40 m to a maximum of ~73 m (Figure 5). The deepened MLD could also be inferred from the temperature and salinity profiles (Figures 6a and 6b). Output from the NASA Ocean Biogeochemical Model (NOBM) showed that the MLD was deeper than 80 m in winters from 1998 to 2007 (http://gdata1.sci.gsfc.nasa.gov/daac-bin/G3/gui.cgi?instance_id=ocean_model_day, *Acker and Leptoukh* [2007]). Forced by strong winds, chlorophyll concentration levels slightly depressed to approximately 0.25 mg m^{-3} (Figure 5). After

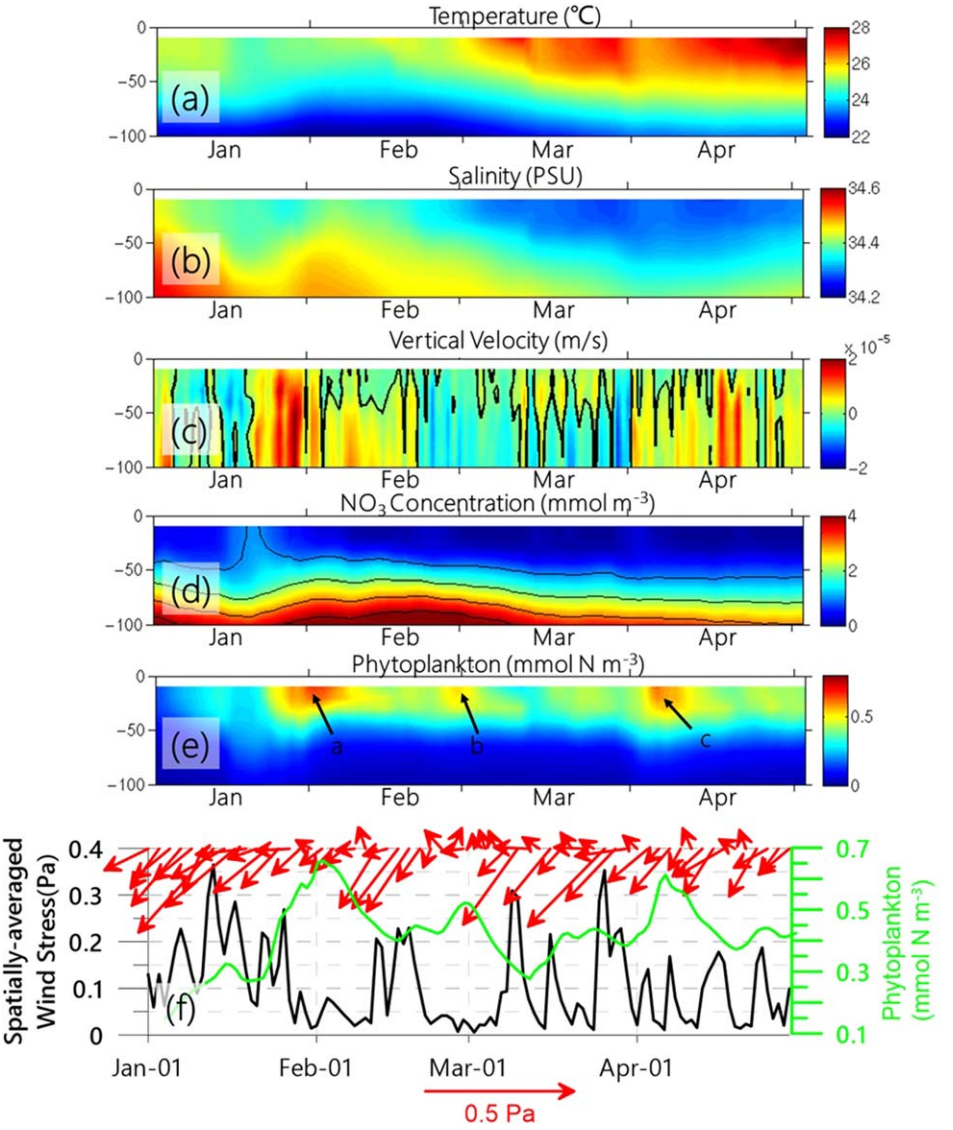

Figure 6. Time-depth map averaged over Box M. (a) temperature, (b) salinity, (c) vertical velocity, (d) NO_3 (in which the contours are values with an interval of 1 mmol m^{-3}) and (e) phytoplankton, respectively. (f) Spatially averaged wind stress (Pa, black curve), surface phytoplankton concentration (mmol N m^{-3}, green curve) and wind vectors (red arrows).

peaking on the 23 January, NO_3 concentration started to decrease while it was taken up by the phytoplankton. Phytoplankton peaked on the 2nd of February with a maximum of ~0.7 mmol N m^{-3} (Figure 6e). Temperature, salinity, and nutrient profiles also showed isoline uplift after the wind intensification. For example, the 34.45 isohaline rose approximately 50 m between 25 and 31 January (Figure 6b).

In addition to the mixing, it was clear that strong, positive vertical motion appeared after 22 January, reaching a high value of $\sim 1.5 \times 10^{-5}$ m s^{-1} (equivalent to 1.3 m d^{-1}, see Figure 6c). This indicated that vertical motion also played a positive role in the nutrient isoline uplift. The generating mechanism of vertical velocity is discussed in next section.

4. Analysis and Discussion

From the results in section 3, the occurrence of the LZB in our model simulation in January 2010 could be identified from high SSC (Figure 2f) distributions, which was consistence with both remote sensing results and the literature [*Shang et al.*, 2012]. In general, the bloom patch had an inverted-V structure that extended for approximately 200 km. The location of the offshore bloom patch was among several major

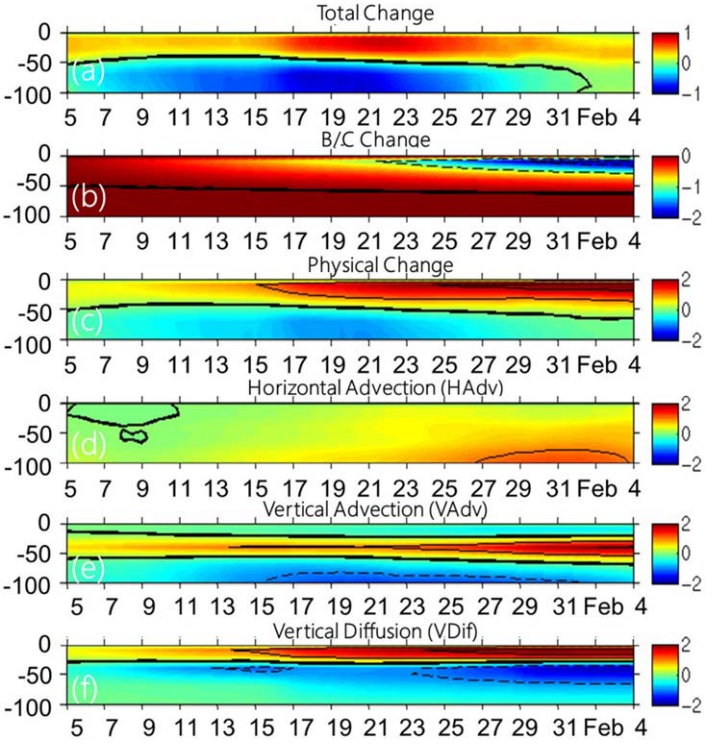

Figure 7. Spatially averaged (over Box M) diagnostic profiles of the terms cumulatively contributing to NO_3 in the upper 100 m of the water column. All terms are integrated over time. Black bold lines indicate zero values. The solid (positive value) and dash (negative value) lines in each subfigure are with an interval of 1.0. Unit for all terms is mmol m^{-3}. (a) Total change rate of NO_3; (b) Contribution from the biological/chemical processes in model (i.e., uptake and nitrification); (c) Total contribution from the physical processes (i.e., vertical and horizontal advection, vertical and horizontal diffusion, while the horizontal diffusion is significantly lower than other three); (d) horizontal advection; (e) vertical advection; and (f) vertical diffusion, respectively.

mesoscale processes: i.e., the Kuroshio loop current, a warm-core eddy, a cold-core eddy, and the LCC. Vertically, high phytoplankton extended down as deep as ~50 m, reaching its maximum average value of ~0.2 mmol N m^{-3} (Figure 6e).

The eddy pumping mechanism was employed to explain this phenomenon [*Shang et al*., 2012]; however, the extent of the bloom patch was much larger than the eddy center region and located further north beyond the eddy center. This implied that mechanisms other than eddy pumping might play essential roles in the dynamics of the bloom patch.

4.1. Ecosystem Responses to Wind

From our model outputs, we computed that within the upper 50 m layer of Box M (Figure 2f), phytoplankton was majorly (~77%) a result of local growth rather than from exterior inputs via horizontal advection. To achieve a better understanding of the nutrient sources sustaining the bloom patch, we diagnosed the nutrient balance in the tracer equation from model outputs. Diagnostically, the temporal variation of nutrient concentration was decomposed into the terms presented in equation (1) [*Shchepetkin and McWilliams*, 2005; *Wang et al*., 2013]:

$$\frac{\partial[NO_3]}{\partial t} = -\left[\frac{\partial(u\cdot[NO_3])}{\partial x} + \frac{\partial(v\cdot[NO_3])}{\partial y}\right] - \left[\frac{\partial(w\cdot[NO_3])}{\partial z}\right] + \left(k_v\cdot\frac{\partial^2[NO_3]}{\partial z^2}\right) + \left(-L_{NO3}\cdot[PHYTO]\right) + \left(L_{nitri}\cdot[NH_4]\right) \quad (1)$$

HAdv | VAdv | VDif | uptake | nitrification

Physical Terms | Biological/Chemical Terms

where u, v, w are velocity components in x, y, and z direction of Cartesian coordinates, and k_v is the vertical diffusion coefficient. L_{NO3} is uptake rate and L_{nitri} is nitrification rate. [*PHYTO*] and [NH_4] represent the concentration of phytoplankton and ammonia, respectively. The first three right-hand side terms are physical terms and last two are biological/chemical terms. The physical terms included the horizontal advection term (HAdv), vertical advection term (VAdv), and vertical diffusion term (VDif). The horizontal diffusion term is 2 orders of magnitude smaller than these other terms, and therefore was neglected in equation (1). The biological/chemical terms included phytoplankton uptake and ammonia nitrification. Time-depth maps of the spatially averaged (within Box M) nitrate budgets terms are presented in Figure 7. The net biological/chemical change (Figure 7b) showed negative values in the upper euphotic layer (~50 m), which was principally dominated by the phytoplankton uptake term. VDif was dominant within surface 40 m layer, with a

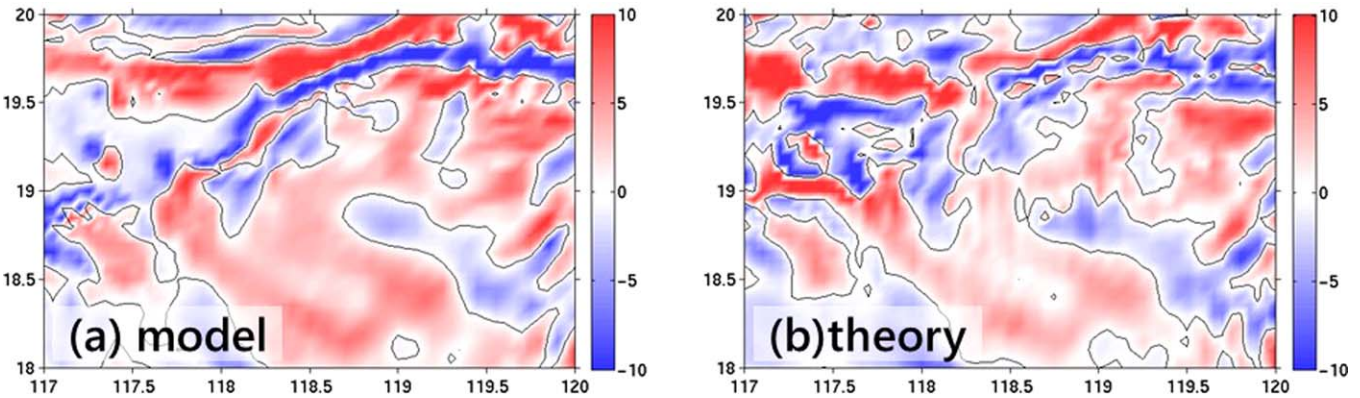

Figure 8. Vertical velocity (unit: m d^{-1}) at 50 m depth from (a) model outputs and (b) that calculated from equation (2). Both are snapshots at 9:00, 28 January 2010. Black contours are zero values.

large value exceeding 2 mmol m^{-3}. A noticeable subsurface VAdv center was seen in Figure 7e, with a maximum at ~45 m. The VDif effect was enhanced and confined to the shallow surface layer (~40 m, >2.0 mmol m^{-3}). The HAdv was relatively small (<0.7 mmol m^{-3}) over the entire 100 m layer. In summary, the biological/chemical processes exhausted nutrients in the upper euphotic layer, especially after 28 January. Vertical diffusion replenished the nutrients in the upper layer, while vertical advection tended to supply nutrients to the subsurface layer. From the simulations, we found that the LZB occurred in the relaxation period just after the wind intensification. The onset of the bloom followed the weakening of the wind. It was shown that the onset of phytoplankton bloom occurred when MLD depth started to shallow, because weakening mixing allowed phytoplankton to accumulate in the surface water [*Townsend et al*., 1992; *Shiozaki et al*., 2014]. Notably, as seen in Figure 7f, wind-induced vertical mixing was the major contributor of nutrients to the upper 40 m of the water column. Vertical mixing in the surface layer began to intensify on 15 January as seen in Figures 5 and 7f. The positive contribution from VDif intensified because of the strengthening of the wind stress (Figure 7f). Both of above evidence suggested that wind-induced mixing variability in the upper layer was responsible for the bloom.

The wind-induced processes can only explain the onset time of the LZB. Because intensified wind was at larger spatial scales than the LZB, it failed to predict the distinctive spatial structure of the LZB. If strengthened mixing was the only mechanism controlling the LZB, the extent of the bloom patch would be larger. Without deep compensation, nutrients in the shallow layer would be rapidly depleted; therefore nutrients were most likely upwelled from the deeper layer (~90 m) into the upper ~30 m layer, where the VDif came into play. Hence, the important role of subsurface upwelling on the LZB was highlighted. The mechanism of the LZB was a two-stage model in which both wind-induced mixing and subsurface upwelling played a role.

In order to examine the practicality of our method in other bloom cases, we also presented depth-time maps beyond January (Figure 6). Three bloom cases were identified (marked a, b, and c in Figure 6e). Each bloom occurred during the relaxation time of the wind and initiate when wind stress starts to weaken (Figure 6f). Case a was the bloom case discussed above. The contrasts among the three cases further support our two-stage model. In Case b, strengthened wind (middle February, Figure 6f) was not sustained by subsurface upwelling, so the intensity of Case b was relatively weak. From mid-February to mid-March, because of negative vertical velocity, nutrients in the upper water were limited and did not allow for a strong bloom. In contrast, although the wind stress was not as strong in Case c as that in Case a and the wind duration was shorter, the intensity of the phytoplankton bloom was stronger than that in Case a because of intense subsurface upwelling.

4.2. Mechanisms of Vertical Velocity

Positive vertical velocity persisted from 22 January to the end of January, with a maximum value of 1.5×10^{-5} m s^{-1} (or 1.3 m d^{-1}, Figure 6c). In regard to the mechanism of subsurface nutrient resupply, Ekman pumping by wind stress curl may have worked to upwell water from deeper layers into the mixed layer [*Wang et al*., 2010]. The magnitude of vertical velocity, w_e, derived from the Ekman pumping was only ~5 m d^{-1} ($w_e = -curl(\tau)/\rho_w f$, where $curl(\tau)$ is the wind stress curl, ρ_w is the density of sea water and f is Coriolis

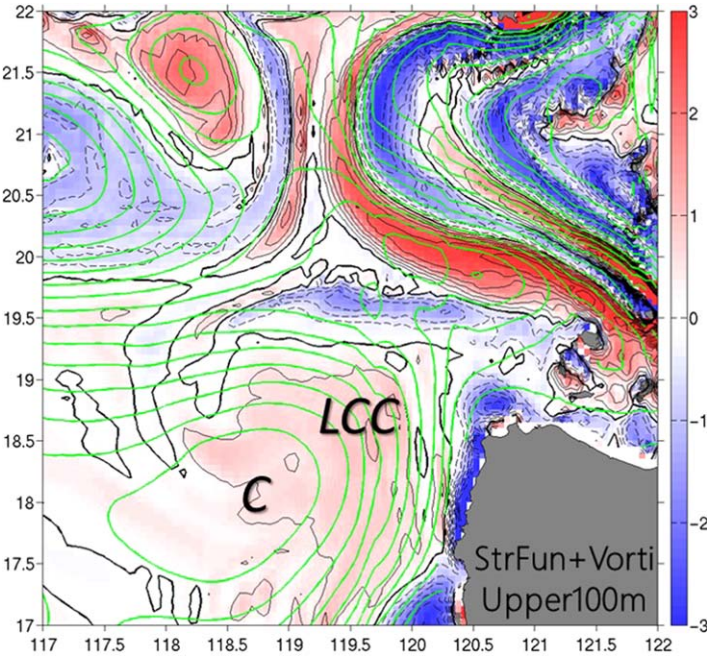

Figure 9. Daily mean upper 100 m averaged relative vorticity (RV) near the LS on 28 January 2010 (shading map, unit: 10^{-5} s^{-1}). The black contours indicate isolines of zero RV and the green contours are the stream function integrated over the upper 100 m (unit: m^2 s^{-1}, with a contour interval of 1.0 m^2 s^{-1}). Black italic abbreviations have the same meaning as those in Figure 1b.

parameter); however, a snapshot of the modeled vertical velocity field at 50 m depth showed that the magnitude could be as large as ~10 m d^{-1} (Figure 8a). Moreover, the wind-induced frictional effects were expected to be confined to the shallower Ekman layer. In addition, the LZB presented a distinct spatial pattern, which did not coincide with the positive Ekman pumping center (Figures 2e and 2f).

The dynamics in the vicinity of the LS were characterized by high relative vorticity (RV, shown in Figure 9). The magnitude of the local Coriolis parameter was $\sim 4 \times 10^{-5}$ s^{-1}, which gave a Rossby number (RV/*f*) of ~0.25; therefore the dynamics may have been in the nonlinear regime. To fully analyze the dynamic mechanisms of vertical velocity, we employed the equation described by *Arthur* [1965], which combined the vorticity equation with the continuity equation. Assuming the vertical velocity at the free surface was zero, the vertically integrated equation could be written as equation (2), which gave the vertical velocity at depth *z* when neglecting the beta effect term, baroclinic term and vortex tilting term:

$$w(z) = \underbrace{-\int_z^\eta \frac{1}{(\zeta+f)}\frac{\partial \zeta}{\partial t}dz}_{\mathrm{WT}} \underbrace{-\int_z^\eta \frac{1}{(\zeta+f)}\vec{v}\cdot\nabla\zeta dz}_{\mathrm{WA}} \underbrace{+\int_z^\eta \frac{1}{(\zeta+f)}A_v\frac{\partial^2\zeta}{\partial z^2}dz}_{\mathrm{WF}} \quad (2)$$

where ζ is the vertical component of RV:

$$\zeta = \frac{\partial v}{\partial x} - \frac{\partial u}{\partial y} \quad (3)$$

In equation (2), the vertical velocity can be decomposed into three terms: the temporal derivative vorticity term (WT), vorticity advection term (WA, and when in combination with WT, total derivative term, WAT) and frictional term (WF). In calculation, a temporal backward difference (1 h backward) and spatial central difference were utilized, and linear interpolation was used to make a rectilinear grid with a spatial resolution of 0.05° from the model's curved grid. In the vertical, linear interpolation was also used to compute vorticity and all other variables to common depth points, with a vertical resolution of 5 m.

Figure 8 depicts a comparison between the vertical velocity derived from model outputs and calculated from equation (2). This comparison showed that the modeled and theoretical vertical velocities were very similar in spatial pattern. At 50 m, the maximum (~10 m d^{-1}) appeared outside the warm-core eddy with a filament-like, submesoscale structure. Observational and modeling studies, such as those in *Klein and Lapeyre* [2009], found similar spatial structures.

In order to present more general temporal variations, using the same technique, each term of the vertical velocity was averaged within Box S in Figure 2f. We chose Box S because the vertical velocity field within

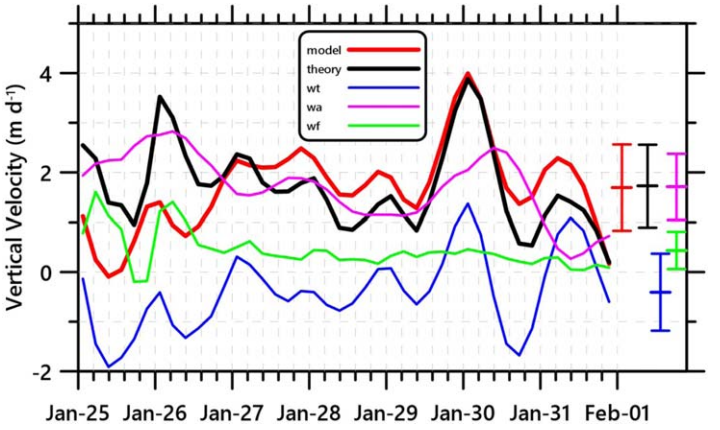

Figure 10. Time series of spatial averaged vertical velocity at 50 m depth within Box S from the model output (red bold) and calculated from equation (2) (black bold). The other curves are the contributions to the vertical velocity from: the temporal derivative of vorticity (WT, blue line), vorticity advection (WA, magenta) and friction (WF, green). Corresponding averaged values and error bars (±1 standard deviation) are shown on the right.

Box S was largely responsible for the subsurface VAdv center. The time series from 25 to 31 January are shown in Figure 10. In Figure 10, the modeled and theoretical vertical velocities agreed well with each other (temporal variability, mean value, and standard deviation). The peak value of 4 m d^{-1} appeared on January 30th. In equation (2), WA was the most important contributor to the vertical velocity, as seen in Figure 10, while averaged WF and WT are lower in magnitude.

The vorticity advection induced strong vertical motion in the northern and northwestern portion of the cold eddy (labeled "*C*" in Figure 9). High lateral RV gradient regions coincided with large vertical velocity, implying that there were contributions from the WA. Along a stream function line of the offshore LCC, the RV changed from large positive values to negative values, which resulted in positive vertical velocity, and vice versa.

In general, the decreases of local vorticity resulted positive vertical velocity, and vice versa. When spatially averaged, the WT possessed large variability. Calculation of the WT term was sensitive to the temporal interval. When calculated from daily output data, the contribution of WT was completely different (not shown in figures). In the detided model, the only daily varying forcing was the surface wind forcing; hence, the temporal variability of the RV field could be explained by adjustments driven by variable winds. Literature also shows that time varying wind will induce time-dependent motions [*D'Asaro*, 1985].

In summary, studying the hydrodynamics from equation (2) showed that vorticity advection played a dominant role in the vertical velocity, while WT and WF had less impact. Although vertical velocity calculated from equation (2) agreed well with the vertical velocity from the model, inconsistencies occurred in the vertical velocity time series (Figure 10). The reasons for the inconsistencies may be because of the following reasons: (1) Computational bias. In the calculation, numerical interpolation methods were applied, which can degrade the signal; (2) Ignored terms, i.e., the vortex tiling term, beta effect term, and baroclinic term, might be important in certain conditions. These may have resulted in an accumulation of computational error.

From the results discussed above, the WA term, which arose from the nonlinear terms in the primitive equations, played the dominant role in driving vertical velocity. Thus, the dynamics of the RV field and flow patterns were the key mechanism of subsurface upwelling. The plane view of the RV presented a complex structure (Figure 9). In the north, interaction of the Kuroshio and the warm-core eddy resulted in a filamentary structure. The warm-core eddy deformed into a narrow filament, which generates another smaller eddy. Meanwhile, high RV differences emerged across the strong Kuroshio front. In the south, a negative RV region existed on the north periphery of the cold-core eddy, which resulted from flow shear. An offshore jet, although smaller in scale, interacted with the ambient circulation and modified the local circulation when flowing offshore. This offshore jet penetrated from the positive RV to the negative RV region and generated high vertical velocity. In summary, vorticity advection resulted from the interaction between the offshore jet and the ambient circulation.

5. Summary

The dynamic mechanism of the LZB was studied with a three-dimensional coupled physical-biological model. The mechanism of the LZB was a two-stage process. Wind-induced mixing stirred subsurface nutrients to surface, while subsurface upwelling maintained nutrient levels from below. Nutrient supply

from vertical mixing was confined to the ~40 m surface layer, while subsurface upwelling advected nutrients from below the mixed layer, which was centered at ~45 m and below. From the hydrodynamic diagnostics, it was found that the main contribution to subsurface upwelling was from vorticity advection (WA), while the temporal variability of vorticity (WT) and the friction term (WF) were smaller. When a spatial average was taken, the magnitude of the vertical velocity, which resulted from the vorticity advection term (WA), was on the order of ~2 m d^{-1}, which approximated the value of modeled vertical velocity. The vorticity advection resulted from an offshore jet's interaction with the RV field determined from the ambient circulation.

The vertical motion in Figure 8 (~19.8°N) presented a finer spatial scale than mesoscale structure, implying that submesoscale processes came into play. Intriguing submesoscale structures were observed when applying the nonlinear Ekman effect [*Niiler*, 1969] on the dynamics of a vortex [*Stern*, 1965] and of a submesoscale ocean front [*Mahadevan*, 2006]; however, the model resolution (~10 km) in this region in the hydrostatic regime was not capable of fully resolving the submesoscale processes. Nevertheless, submesoscale processes would drastically modify the upwelling process, which is beyond the scope of this study. Abundant eddy and frontal activities in the SCS provide many scenarios for in-depth discussion about the effects of submesoscale processes and their role in the biogeochemical system, which are deserving of future simulation and exploration.

Acknowledgments

This work was supported by grant (2013CB955704) from the National Basic Research Program of China; grant (41476005) from the Natural Science Foundation of China (NSFC); grant (U1305231) from NSFC and Fujian Province. Details for the remote sensing and other data utilized in this paper are described in section 2. To request model outputs, please sent e-mail to Wenfang Lu (scenty2886@gmail.com). Part of the analyses used in this paper was produced with the Giovanni online data system, developed and maintained by the NASA GES DISC. Special thanks are given to Shaoling Shang for the remote sensing images she offered.

References

Acker, J. G., and G. Leptoukh (2007), Online analysis enhances use of NASA Earth science data, *Eos Trans. AGU*, *88*(2), 14–17, doi:10.1029/2007EO020003.

Arthur, R. S. (1965), On the calculation of vertical motion in eastern boundary currents from determinations of horizontal motion, *J. Geophys. Res.*, *70*(12), 2799–2803.

Caruso, M. J., G. G. Gawarkiewicz, and R. C. Beardsley (2006), Interannual variability of the Kuroshio intrusion in the South China Sea, *J. Oceanogr.*, *62*(4), 559–575, doi:10.1007/s10872-006-0076-0.

Chelton, D. B., R. A. deSzoeke, M. G. Schlax, K. El Naggar, and N. Siwertz (1998), Geographical variability of the first baroclinic Rossby radius of deformation, *J. Phys. Oceanogr.*, *28*(3), 433–460, doi:10.1175/1520-0485(1998)028<0433:GVOTFB>2.0.CO;2.

Chen, C.-C., F.-K. Shiah, S.-W. Chung, and K.-K. Liu (2006), Winter phytoplankton blooms in the shallow mixed layer of the South China Sea enhanced by upwelling, *J. Mar. Syst.*, *59*(1–2), 97–110, doi:10.1016/j.jmarsys.2005.09.002.

Chen, Y.-L. L., H.-Y. Chen, I.-I. Lin, M.-A. Lee, and J. Chang (2007), Effects of cold eddy on phytoplankton production and assemblages in Luzon Strait bordering the South China Sea, *J. Oceanogr.*, *63*(4), 671–683.

D'Asaro, E. A. (1985), The energy flux from the wind to near-inertial motions in the surface mixed layer, *J. Phys. Oceanogr.*, *15*(8), 1043–1059.

Fang, G., W.-d. Fang, Y. Fang, and K. Wang (1998), A survey of studies on the South China Sea upper ocean circulation, *Acta Oceanogr. Taiwan.*, *37*, 1–16.

Fennel, K., J. Wilkin, J. Levin, J. Moisan, J. O'Reilly, and D. Haidvogel (2006), Nitrogen cycling in the Middle Atlantic Bight: Results from a three-dimensional model and implications for the North Atlantic nitrogen budget, *Global Biogeochem. Cycles*, *20*, GB3007, doi:10.1029/2005GB002456.

Hu, J., H. Kawamura, H. Hong, and Y. Qi (2000), A review on the currents in the South China Sea: Seasonal circulation, South China Sea Warm Current and Kuroshio intrusion, *J. Oceanogr.*, *56*(6), 607–624, doi:10.1023/A:1011117531252.

Jiang, Y. W., F. Chai, Z. W. Wan, X. Zhang, and H. S. Hong (2011), Characteristics and mechanisms of the upwelling in the southern Taiwan Strait: A three-dimensional numerical model study, *J. Oceanogr.*, *67*(6), 699–708, doi:10.1007/s10872-011-0080-x.

Klein, P., and G. Lapeyre (2009), The oceanic vertical pump induced by mesoscale and submesoscale turbulence, *Annu. Rev. Mar. Sci.*, *1*(1), 351–375, doi:10.1146/annurev.marine.010908.163704.

Liao, E., Y. Jiang, L. Li, H. Hong, and X. Yan (2013), The cause of the 2008 cold disaster in the Taiwan Strait, *Ocean Modell.*, *62*, 1–10, doi:10.1016/j.ocemod.2012.11.004.

Liu, K. K., S. Y. Chao, P. T. Shaw, G. C. Gong, C. C. Chen, and T. Y. Tang (2002), Monsoon-forced chlorophyll distribution and primary production in the South China Sea: Observations and a numerical study, *Deep Sea Res., Part I*, *49*(8), 1387–1412, doi:10.1016/s0967-0637(02)00035-3.

Mahadevan, A. (2006), Modeling vertical motion at ocean fronts: Are nonhydrostatic effects relevant at submesoscales?, *Ocean Modell.*, *14*(3-4), 222–240, doi:10.1016/j.ocemod.2006.05.005.

Mellor, G. L., and T. Yamada (1982), Development of a turbulence closure model for geophysical fluid problems, *Rev. Geophys.*, *20*(4), 851–875, doi:10.1029/RG020i004p00851.

Metzger, E. J., and H. E. Hurlburt (2001), The Nondeterministic Nature of Kuroshio Penetration and Eddy Shedding in the South China Sea, *J. Phys. Oceangr.*, *31*(7), 1712–1732.

Nan, F., H. Xue, F. Chai, L. Shi, M. Shi, and P. Guo (2011), Identification of different types of Kuroshio intrusion into the South China Sea, *Ocean Dynamics*, *61*(9), 1291–1304, doi:10.1007/s10236-011-0426-3.

Niiler, P. P. (1969), On the Ekman divergence in an oceanic jet, *J. Geophys. Res.*, *74*(28), 7048–7052, doi:10.1029/JC074i028p07048.

Peñaflor, E. L., C. L. Villanoy, C.-T. Liu, and L. T. David (2007), Detection of monsoonal phytoplankton blooms in Luzon Strait with MODIS data, *Remote Sens. Environ.*, *109*(4), 443–450.

Shang, S., L. Li, J. Li, Y. Li, G. Lin, and J. Sun (2012), Phytoplankton bloom during the northeast monsoon in the Luzon Strait bordering the Kuroshio, *Remote Sens. Environ.*, *124*, 38–48, doi:10.1016/j.rse.2012.04.022.

Shaw, P.-T., S.-Y. Chao, K.-K. Liu, S.-C. Pai, and C.-T. Liu (1996), Winter upwelling off Luzon in the northeastern South China Sea, *J. Geophys. Res.*, *101*(C7), 16,435–16,448, doi:10.1029/96JC01064.

Shchepetkin, A. F., and J. C. McWilliams (2005), The regional oceanic modeling system (ROMS): A split-explicit, free-surface, topography-following-coordinate oceanic model, *Ocean Modell.*, *9*(4), 347–404, doi:10.1016/j.ocemod.2004.08.002.

Shiozaki, T., S.-I. Ito, K. Takahashi, H. Saito, T. Nagata, and K. Furuya (2014), Regional variability of factors controlling the onset timing and magnitude of spring algal blooms in the northwestern North Pacific, *J. Geophys. Res. Oceans*, *119*, 253–265, doi:10.1002/2013JC009187.

Stern, M. E. (1965), Interaction of a uniform wind stress with a geostrophic vortex, *Deep Sea Res. Oceanogr. Abstr.*, *12*(3), 355–367, doi: 10.1016/0011-7471(65)90007-0.

Sverdrup, H. (1953), On conditions for the vernal blooming of phytoplankton, *J. Cons.*, *18*(3), 287–295.

Tang, D.-L., I.-H. Ni, D. R. Kester, and F. E. Muller-Karger (1999), Remote sensing observations of winter phytoplankton blooms southwest of the Luzon Strait in the South China Sea, *Mar. Ecol. Prog. Ser.*, *191*, 43.

Townsend, D. W., M. D. Keller, M. E. Sieracki, and S. G. Ackleson (1992), Spring phytoplankton blooms in the absence of vertical water column stratification, *Nature*, *360*(6399), 59–62.

Wang, G., J. Su, and P. C. Chu (2003), Mesoscale eddies in the South China Sea observed with altimeter data, *Geophys. Res. Lett.*, *30*(21), 2121, doi:10.1029/2003GL018532.

Wang, G., D. Wang, and T. Zhou (2012), Upper layer circulation in the Luzon Strait, *Aquat. Ecosyst. Health Manage.*, *15*(1), 39–45.

Wang, G. H., D. Chen, and J. L. Su (2008), Winter eddy genesis in the eastern south china sea due to orographic wind jets, *J. Phys. Oceanogr.*, *38*(3), 726–732, doi:10.1175/2007jpo3868.1.

Wang, J., H. Hong, Y. Jiang, F. Chai, and X.-H. Yan (2013), Summer nitrogenous nutrient transport and its fate in the Taiwan Strait: A coupled physical-biological modeling approach, *J. Geophys. Res. Oceans*, *118*, 4184–4200, doi:10.1002/jgrc.20300.

Wang, J. J., D. L. Tang, and Y. Su (2010), Winter phytoplankton bloom induced by subsurface upwelling and mixed layer entrainment southwest of Luzon Strait, *J. Mar. Syst.*, *83*(3-4), 141–149, doi:10.1016/j.jmarsys.2010.05.006.

Wong, G. T. F., T. L. Ku, M. Mulholland, C. M. Tseng, and D. P. Wang (2007), The SouthEast Asian time-series study (SEATS) and the biogeochemistry of the South China Sea—An overview, *Deep Sea Res., Part II*, *54*(14-15), 1434–1447, doi:10.1016/j.dsr2.2007.05.012.

Wu, C.-R., and T.-L. Chiang (2007), Mesoscale eddies in the northern South China Sea, *Deep Sea Res., Part II*, *54*(14-15), 1575–1588, doi: 10.1016/j.dsr2.2007.05.008.

Wu, C.-R., and Y.-C. Hsin (2012), The forcing mechanism leading to the Kuroshio intrusion into the South China Sea, *J. Geophys. Res.*, *117*, C07015, doi:10.1029/2012JC007968.

Wyrtki, K. (1961), Physical oceanography of the Southeast Asian waters, *NAGA Rep. 2*, 195 pp., Scripps Inst. of Oceanogr., Univ. of Calif., San Diego.

Xiu, P., F. Chai, L. Shi, H. Xue, and Y. Chao (2010), A census of eddy activities in the South China Sea during 1993–2007, *J. Geophys. Res.*, *115*, C03012, doi:10.1029/2009JC005657.